Chemical Engineering Science 275 (2023) 118748

Contents lists available at ScienceDirect

Chemical Engineering Science

journal homepage: www.elsevier.com/locate/ces

Promoting propane dehydrogenation over PtFe bimetallic catalysts by optimizing the state of Fe species

Kai Bian [a], Guanghui Zhang [a,*], Mingrui Wang [a], Shida Liu [b], Christian J. Breckner [c], David P. Dean [c], Jie Zhu [a], Jeffrey T. Miller [c], Shuandi Hou [b,*], Chunshan Song [a,d], Xinwen Guo [a,*]

[a] State Key Laboratory of Fine Chemicals, Frontier Science Center for Smart Materials, School of Chemical Engineering, Dalian University of Technology, Dalian 116024, PR China
[b] Sinopec Dalian (Fushun) Research Institute of Petroleum and Petrochemicals, Dalian 116045, PR China
[c] Charles D. Davidson School of Chemical Engineering, Purdue University, 480 Stadium Mall Drive, West Lafayette, IN 47907, USA
[d] Department of Chemistry, Faculty of Science, the Chinese University of Hong Kong, Shatin, NT, Hong Kong, PR China

ARTICLE INFO

Keywords:
Propane dehydrogenation reaction
PtFe bimetallic catalysts
Structural optimization
The state of Fe species

ABSTRACT

Optimizing the structure of Pt-based bimetallic catalysts is of utmost importance toward improving the propane dehydrogenation performance. It is challenging to precisely synthesize uniform PtFe alloy nanoparticles without excess unalloyed Fe species on the support as these Fe species lead to low propylene selectivity, coke deposition, and poor stability. Herein, we report an effective strategy to optimize the structure of PtFe bimetallic catalysts with minimal coke and high turnover frequency (8.2 s^{-1}). For the optimized catalyst, 1Pt3Fe@S-1, most Fe species is in the framework of the zeolite S-1, which significantly suppresses the formation of coke. In addition, the extra-framework Fe and Pt species encapsulated in the channel of zeolite form uniform PtFe alloy nanoparticles, which significantly improves the C_3H_6 selectivity, catalytic stability, and recycling performance. These findings provide insights into the structure-performance relationship of PtFe bimetallic catalysts and shall be beneficial to future design and optimization of similar catalytic materials.

1. Introduction

Pt-based catalysts have been widely used in the industrial propane dehydrogenation (PDH) process because of their low toxicity, superior activation of C–H bonds, and suppression of C–C bond cleavage (Atanga et al., 2018; Carter et al., 2021; Chen et al., 2021a; Chen et al., 2020; Dai et al., 2021a; Liu et al., 2021; Sattler et al., 2014b; Wang et al., 2023; Yang et al., 2018). The introduction of promoters into Pt-based catalysts is an effective strategy to combat the formation of coke and significantly improves the stability and C_3H_6 selectivity. Various 3d-transition metals and main group metals, such as V (Purdy et al., 2020), Cr (LiBretto et al., 2019), Mn (Fan et al., 2020; Liu et al., 2022; Rochlitz et al., 2022; Wu et al., 2018), Fe (Bian et al., 2022; Wegener et al., 2020), Co (Cesar et al., 2019), Cu (Han et al., 2014; Li et al., 2018; Sun et al., 2018), Zn (Chen et al., 2021b; Cybulskis et al., 2017; Rochlitz et al., 2019; Sun et al., 2020), Ga (Nakaya et al., 2021; Searles et al., 2018; Wang et al., 2022b; Zhang et al., 2021), Sn (Chen et al., 2021c; Liu et al., 2019a; Liu et al., 2019b; Lobera et al., 2010; Shi et al., 2015; Xiong et al., 2017; Yang et al., 2012; Zhang et al., 2019), In (Escorcia et al., 2020; Sripinun et al., 2021), Sb (Ye et al., 2018), Bi (Zhu Chen et al., 2019), etc., have been studied as promoters. Catalytic structures of intermetallic compound (IMC), single atom alloy (SAA) and core–shell bimetallic alloy have been successfully synthesized. The addition of promoters separates the multi-Pt ensembles, which inhibits the structure-sensitive side reactions, including hydrogenolysis and carbon deposition (Chen et al., 2021c; Xiong et al., 2017; Zhang et al., 2019). From the aspect of electronic effect, alloying modulates the orbital energy of Pt, which changes the heats of adsorption/desorption for propylene and/or intermediate species on the active sites and suppresses the deep dehydrogenation to form coke (Cybulskis et al., 2017; Sun et al., 2020; Ye et al., 2018).

When group VIII (Fe, Co, and Ni) promoters are used in Pt-based bimetallic catalysts, an excessive amount of the promoter is usually added (Dai et al., 2021b; Estes et al., 2016; Hu et al., 2015; Hu et al., 2022; Yang et al., 2020; Zhang et al., 2018a). For instance, Wegener *et al.* compared the catalytic performance of PtFe IMCs in PDH reaction, where the PtFe alloy with an Fe-rich structure showed a higher C_3H_6 formation rate (Wegener et al., 2020). However, the excessive amount of Fe species forms unalloyed metallic Fe nanoparticles during reduction

* Corresponding authors.
E-mail addresses: gzhang@dlut.edu.cn (G. Zhang), houshuandi.fshy@sinopec.com (S. Hou), guoxw@dlut.edu.cn (X. Guo).

https://doi.org/10.1016/j.ces.2023.118748
Received 28 February 2023; Received in revised form 30 March 2023; Accepted 8 April 2023
Available online 13 April 2023

and PDH reaction, which promotes the hydrogenolysis and carbon deposition reactions (Bian et al., 2022; Pérez-Ramírez et al., 2004; Wang et al., 2019; Yang et al., 2020). Precisely synthesizing well-defined and uniform alloy sites while eliminating the excessive unalloyed promoters have been challenging for the development of Pt-based PDH catalysts with group VIII promoters, and numerous efforts have been made to address this. Cai et. al. prepared a core–shell structure of Pt@PtM alloy by acid treatment of PtM (M = Fe, Co, and Ni) bimetallic catalysts (Cai et al., 2018). The Fe, Co and Ni on the surface of the catalysts are removed during the acid treatment, which suppresses the side reactions such as coking and cracking. These results have shown the potential impact of fine-tuning the surface structure on improving the catalytic performance and inhibiting the formation of coke. In addition, we previously reported another strategy to optimize the PtFe bimetallic structure by introducing the soft oxidant of CO_2 to PDH process (Bian et al., 2022). The coking active sites of unalloyed metallic Fe species are selectively oxidized to Fe_3O_4 under reaction conditions, which significantly inhibits the carbon deposition. Meanwhile, the preserved PtFe alloy shows a high C_3H_6 selectivity. One drawback of this strategy is that propane and CO_2 may competitively adsorb on the catalytic surface, which leads to a decreased C_3H_6 formation rate. Therefore, it is desirable to develop other strategies to further optimize the structure of PtFe bimetallic catalysts to achieve better PDH catalytic performance without using CO_2.

Herein, we report another effective tactic to optimize the structure of PtFe bimetallic catalysts by tuning the state of Fe species, which significantly improves the PDH performance. Based on the previous understanding of PtFe bimetallic catalyst for the PDH reaction, the formation of coke can be significantly inhibited by transforming the excess unalloyed metallic Fe species into FeO_x species (Yang et al., 2020). In addition, Liu found that the Fe species can get integrated into the framework of the zeolite during synthesis and in turn anchor the noble metal species to form isolated Pt sites (Liu et al., 2023), providing opportunities to prepare high performance PDH catalyst with ultra-small Pt cluster. In this manuscript, we focus on the structural optimization of PtFe bimetallic alloy. Three PtFe bimetallic catalysts with different structures were synthesized, among which the presence of both framework and extra-framework Fe species leads to the significantly inhibited coke deposition and long-term stability.

2. Experimental section

2.1. Catalyst Synthesis

Pt/S-1 and 1Pt7Fe/S-1: The Silicalite-1 support (S-1) was synthesized via the hydrothermal crystallization method at 170 ℃ for 3 days with a molar ratio of 1 tetraethyl orthosilicate (TEOS): 0.27 tetrapropylammonium hydroxide (TPAOH): 35 H_2O in the precursor (Dai et al., 2015). After washing and centrifugation, the product was dried at 100 ℃ and calcined at 540 ℃ for 6 h in air to remove the template, denoted as S-1. 1.0 wt% of Fe and/or 0.5 wt% of Pt were sequentially introduced onto the S-1 support via the charge enhanced dry impregnation (CEDI) method (Yang et al., 2019). For example, 1.0 wt% of Fe was loaded onto S-1, and after drying and calcination at 400 ℃ for 4 h, the product was obtained and denoted as Fe/S-1. 0.5 wt% of Pt was then impregnated onto the S-1 or Fe/S-1 samples, and after drying and calcination at 250 ℃ for 4 h, these samples were obtained and denoted as Pt/S-1 and 1Pt7Fe/S-1 (the molar ratio of Pt/Fe is 1:7), respectively.

1Pt@7FeS-1: The FeS-1 (1.0 wt% of Fe) and 1Pt@7FeS-1(1.0 wt% of Fe, 0.5 wt% of Pt) catalysts were synthesized *in-situ* via the hydrothermal crystallization method, and the detailed procedures are as follows. 16.5 g of TEOS, 17.5 g of 25 wt% TPAOH solution and 31.0 mL of H_2O were mixed and stirred for 3 h. 1.05 g of H_2PtCl_6 solution (0.06 wt%) mixed with 0.18 g of ethylenediamine was added dropwise into the solution and stirred for 1 h. Then 0.29 g of EDTA-2Na and 0.34 g of Fe $(NO_3)_3{\cdot}9H_2O$ were both completely dissolved in 3 mL of H_2O, and added dropwise into the mixture solution and stirred for 1 h. The final solution was crystallized at 170 ℃ for 3 days. After centrifugation, washing and drying overnight at 100 ℃, these products were denoted as FeS-1 and 1Pt@7FeS-1 (the molar ratio of Pt/Fe is 1:7), respectively.

Pt@S-1 and xPtyFe@S-1: The synthesis processes of Pt@S-1 (0.5 wt % of Pt) and xPtyFe@S-1 are similar. In a typical synthesis process (1.0 wt% of Fe, 0.5 wt% of Pt), the solution containing ethylenediamine and H_2PtCl_6 was added dropwise into the Si-containing solution and stirred for 1 h. Then 0.18 g of ethylenediamine was added into 3 mL of the solution with 0.34 g of $Fe(NO_3)_3{\cdot}9H_2O$, and was quickly added dropwise into the Si-containing solution and stirred for 1 h. The final solution was transferred into a steel autoclave and crystallized at 170 ℃ for 3 days. After centrifugation, washing and drying overnight at 100 ℃, these products were denoted as Pt@S-1 and xPtyFe@S-1 (the x/y represents the molar ratio of Pt/Fe, such as 3Pt1Fe, 1Pt1Fe, 1Pt3Fe and 1Pt7Fe), respectively.

2.2. Catalytic testing

The catalytic reactions were carried out in a fixed-bed reactor. 0.15 g of catalyst powder was placed in the isothermal zone of a quartz tube reactor with an inner diameter of 8 mm. Each catalyst was first reduced with pure H_2 (30 mL/min) at 550 ℃ for 1 h and purged with pure N_2 (30 mL/min) for 15 min. The reactant gas (C_3H_8/N_2 = 1:7) was then continuously fed into the reactor, and the gas hourly space velocity (GHSV) was maintained at 16000 $mL{\cdot}h^{-1}{\cdot}g_{cat}^{-1}$. The PDH reaction was performed at 550 ℃ and ambient pressure. During the successive oxidation–reduction PDH test, each cycle includes a step of PDH for 5 h, followed by a treatment in air (30 mL/min) at 550 ℃ for 0.85 h to remove the deposited coke and then reduction via pure H_2 (30 mL/min) at 550 ℃ for 0.5 h. The products were analyzed by using an online gas chromatography integrated with double detectors: a Thermal Conductivity Detector (TCD) for N_2 and CH_4, and a Flame Ionization Detector (FID) for hydrocarbons, including CH_4, C_2H_6, C_2H_4, C_3H_8, C_3H_6, C_4H_{10}, C_4H_8 and C_4H_6. The conversion of C_3H_8 (X_{C3H8}), selectivity of hydrocarbon product i (S_i) and carbon balance (B_{C3H8}) were calculated according to Eqs. (1) to (3). The turnover frequency (TOF_{C3H6}) and deactivation constant (K_d) of 1Pt3Fe@S-1 were calculated via Eqs. (4) and (5) respectively.

$$X_{C3H8} = \frac{n_{C3H8,in} - n_{C3H8,out}}{n_{C3H8,in}} \times 100\% \tag{1}$$

$$S_i = \frac{m_i \times n_{i,out}}{3 \times \left(n_{C3H8,in} - n_{C3H8,out}\right)} \times 100\% \tag{2}$$

$$B_{C3H8} = \frac{\sum_{i=1}^{4} m_i \times n_{i,out}}{3 n_{C3H8,out}} \times 100\% \tag{3}$$

$$TOF_{C3H6} = \frac{F_{C3H8} \times X_{C3H8} \times S_{C3H6} \times 195.1}{22.4 \times 60 \times m_{cat} \times 0.5\,wt\% \times D_{Pt}} s^{-1} \tag{4}$$

$$K_d = \frac{ln\left(\frac{1-X_{final}}{X_{final}}\right) - ln\left(\frac{1-X_{initial}}{X_{initial}}\right)}{t} h^{-1} \tag{5}$$

where $n_{C3H8,in}$ and $n_{C3H8,out}$ represent the molar concentration of C_3H_8 in feed and effluent, respectively; $n_{i,out}$ represents the molar concentration of product i and m_i represents the number of carbon atoms; F_{C3H8} represents the flow rate of C_3H_8 and t represents the duration of long-term PDH reaction in hours.

2.3. Characterization

A Rigaku Smartlab 9 kW X-ray diffractometer equipped with Cu Kα radiation was used to characterize the crystalline structure for the reduced samples (treated in pure H_2 at 550 °C for 1 h). The pore structure was determined by Ar adsorption–desorption on a

Quantachrome AUTOSORB-1-MP sorption analyzer at −186 °C. Prior to the measurements, the reduced samples were degassed at 300 °C for 6 h. The specific surface area and micropore volume were calculated using the Brunauer-Emmet-Teller (BET) and Saito-Foley (SF) model, respectively, and the total pore volume was estimated at $P/P_0 = 0.99$. The high-resolution transmission electron microscopy (HR-TEM), high angle annular dark field-scanning TEM (HADDF-STEM) and energy dispersive spectrometer (EDS) images were obtained on an FEI Tecnai F30 instrument, and the samples were prepared using ethanol suspension of reduced samples dispersed on copper grids. UV-Raman measurements were carried out using a 266 nm excitation source to characterize the framework Fe species. UV–Vis spectra were collected on a Jasco UV-550 spectrometer to investigate the Fe species in PtFe bimetallic catalysts and the hydrogenation product of 3-Nitrotoluene with $NaBH_4$. The content of Pt, extra-framework Fe and framework Fe species were determined respectively by inductively coupled plasma optical emission spectrometry (ICP-OES) on a PerkinElmer AVIO 500 instrument. The Fe species dissolved by dilute HNO_3 (10 vol%) were considered as the extra-framework Fe species and its amount was determined using ICP analysis. After removing the extra-framework Fe species, HF and aqua regia were both added to dissolve the framework Fe and Pt species for ICP analysis. The ^{57}Fe Mössbauer spectra of reduced samples were measured on a Topologic 500A spectrometer and a proportional counter at room temperature. ^{57}Co (Rh) moving in a constant acceleration mode was used as a radioactive source. The *in-situ* X-ray absorption spectroscopy (XAS) measurements were conducted on the bending magnet beamline of the Materials Research Collaborative Access Team (MR-CAT) at the Advanced Photon Source (APS), Argonne National Laboratory at the Pt L_{III} Edge (11,564.0 eV) and the Fe K edge (7,112.0 eV). All the samples were pre-treated at 550 °C with 5% H_2 in He, and the spectra were collected at room temperature in He post-reduction without exposure to air. The *in-situ* CO diffuse reflectance infrared Fourier transform spectra (CO-Drifts) were collected on a Thermo Nicolet iS50 spectrometer with a mercury cadmium telluride (MCT) detector cooled by liquid nitrogen. Prior to the test, the sample was reduced at 550 °C and ambient pressure under pure H_2 for 1 h. After that the reduced sample was exposed to 10 vol% of CO/N_2 at 30 °C for 30 min, and the spectra were collected after purging with N_2 for 30 min. X-ray photoelectron spectroscopy (XPS) was performed over a spectrometer (Model Max 200, Leybold, Germany) using Al Kα radiation as an excitation source. Vis-Raman spectroscopy was performed to investigate the coke formation for the spent samples on a DL-2 microscopic Raman spectrometer with a 532 nm Ar-ion laser beam. Thermogravimetric analysis (TGA) was obtained on an SDT Q600 apparatus to measure the carbon deposition of the spent catalysts, scanning from 30 to 800 ℃ with a heating rate of 10 ℃/min in air. H_2-temperature-programmed reduction (H_2-TPR), NH_3-temperature-programmed desorption (NH_3-TPD), and volumetric CO chemisorption experiments were carried out on a Quantachrome ChemBET Pulsar analyzer. Before the test, about 0.1 g of the sample was pretreated in He at 400 °C for 1 h and then cooled to 30 °C. For the H_2-TPR test, the 1Pt7Fe/S-1 and reduced 1Pt7Fe@S-1 as well as 1Pt@7FeS-1 were tested from 30 to 900 °C with a ramp rate of 10 °C/min in 5 vol% H_2/Ar. For the NH_3-TPD test, the reduced catalysts were pre-adsorbed with 8 vol% NH_3/He for 30 min at 120 °C and purged by pure He before conducting TPD from 120 to 650 ℃ at 10 ℃/min. For the volumetric CO chemisorption, 0.15 g of reduced 1Pt3Fe@S-1 (m_{sam}) was tested at room temperature, and the dispersion of Pt species (D_{Pt}) was calculated by the adsorbed volume of CO ($V_{CO} = 23$ μL) in Eq. (6).

$$D_{Pt} = \frac{V_{co} \times 195.1}{22.4 \times 0.5\,\text{wt\%} \times m_{sam}} \times 100\% \quad (6)$$

3. Results and discussion

3.1. Structure design and characterization

To optimize the structure of the Fe species, three synthetic methods were proposed. In the previous work (Bian et al., 2022), the catalyst with low Pt/Fe ratio (Pt/Fe = 1:7) showed the highest stability and propylene yield than the other PtFe bimetallic catalysts in the steady state, since it has sufficient Fe atoms around the Pt species, which makes it easier to form the PtFe alloy highly active for PDH. Thus 1Pt7Fe/S-1 was synthesized using a similar method, where PtFe alloy and Fe(0) nanoparticles are both expected. In the presence of EDTA with strong complexing ability, the coordinated Fe species tends to integrate into the framework of the zeolite during the synthesis (Yang et al., 2020), and thus Pt and framework FeO_x are expected in 1Pt@7FeS-1. It is noteworthy that high PDH activity and selectivity require PtFe alloy nanoparticles, instead of Pt(0) nanoparticles, so we next synthesized 1Pt7Fe@S-1, where ethylenediamine was used during the synthesis, aiming to obtain both framework Fe and extra-framework Fe, the latter of which is expected to be uniformly dispersed and alloyed with Pt during the reduction step (Scheme 1).

To verify our hypotheses and investigate the states of Fe species, a series of characterizations to determine Fe speciation were carried out. As shown in the Fig. 1**A and 1B**, minimal framework Fe species (520, 1020, 1120 and 1172 cm^{-1}) was observed in the UV-Raman spectrum of 1Pt7Fe/S-1, while it is present in 1Pt@7FeS-1 and 1Pt7Fe@S-1 (Dai et al., 2016; Fan et al., 2009). After H_2 reduction, the framework iron species remains. Besides, a wide band from 300 to 700 nm in the UV–Vis spectra was observed on 1Pt7Fe/S-1, as shown in Fig. 1**C**, which could be attributed to extra-framework Fe species, such as Fe_2O_3 nanoparticles (Lari et al., 2015; Luo et al., 2016). There is no absorption peak in this range for 1Pt@7FeS-1. A sharp peak appears below 300 nm, which typically corresponds to the vibration of tetrahedrally coordinated framework Fe species (Yang et al., 2020). For 1Pt7Fe@S-1, both framework and extra-framework Fe species were observed. After H_2 reduction, the signal of extra-framework Fe species in 1Pt7Fe/S-1 and 1Pt7Fe@S-1 decreased, as shown in Fig. 1**D**. However, the framework Fe species of 1Pt@7FeS-1 and 1Pt7Fe@S-1 remained, without observable reduction peaks in H_2-TPR (**Fig. S1A**), which is in accordance with the UV-Raman results. In addition, the ICP results show similar Pt content among the three PtFe bimetallic catalysts, but the content of Fe species is significantly different. 0.95 wt% of Fe species was determined using the dilute HNO_3 treatment in Table 1, indicating that most of the Fe species on 1Pt7Fe/S-1 are extra-framework. No extra-framework Fe species was detected with the dilute HNO_3 treatment on 1Pt@7FeS-1, while 0.96 wt % of Fe species was determined using the HF and aqua regia pickling, indicating that the majority of the Fe species is in the zeolite framework. 0.05 wt% of extra-framework Fe and 0.88 wt% of framework Fe were determined for 1Pt7Fe@S-1, which consists with the mixed states of Fe species in UV–Vis.

The Mössbauer spectra are shown in Fig. 2, and the fitting results are displayed in **Table S1**. The reduced 1Pt7Fe/S-1 contains superparamagnetic Fe^{3+}, Fe^{2+} and large amounts of metallic Fe^0 species (39.2%) in Fig. 2**A** (Bian et al., 2022; Fierro et al., 2011; Zhu et al., 2022). Metallic Fe^0 species are absent in 1Pt@7FeS-1, while the superparamagnetic Fe^{3+} species is observed, as shown in Fig. 2**B**, which implies that most of the Fe species remains stable in the framework of zeolite after H_2 reduction (Luo et al., 2016). For the reduced 1Pt7Fe@S-1, a majority of FeO_x and small amount of metallic Fe species (3.3%) were both detected (Fig. 2**C**), which agrees with the UV–Vis and ICP results. These results demonstrate that the states of Fe species among three reduced PtFe bimetallic catalysts are significantly different via tuning the synthesis methods.

To investigate the electronic structure and coordination environment of the Pt and Fe species, the PtFe bimetallic catalysts were analyzed using *in-situ* XAS and CO-Drifts in Fig. 3. The *in-situ* Fe K edge XANES

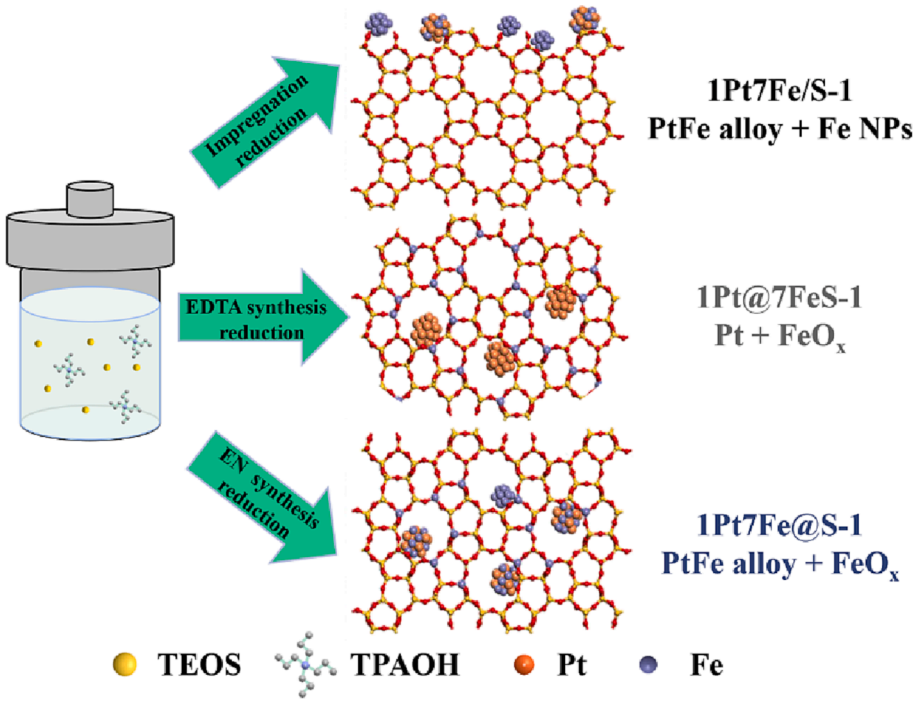

Scheme 1. Structural conjecture of three PtFe bimetallic catalysts with different Fe distribution and states after reduction.

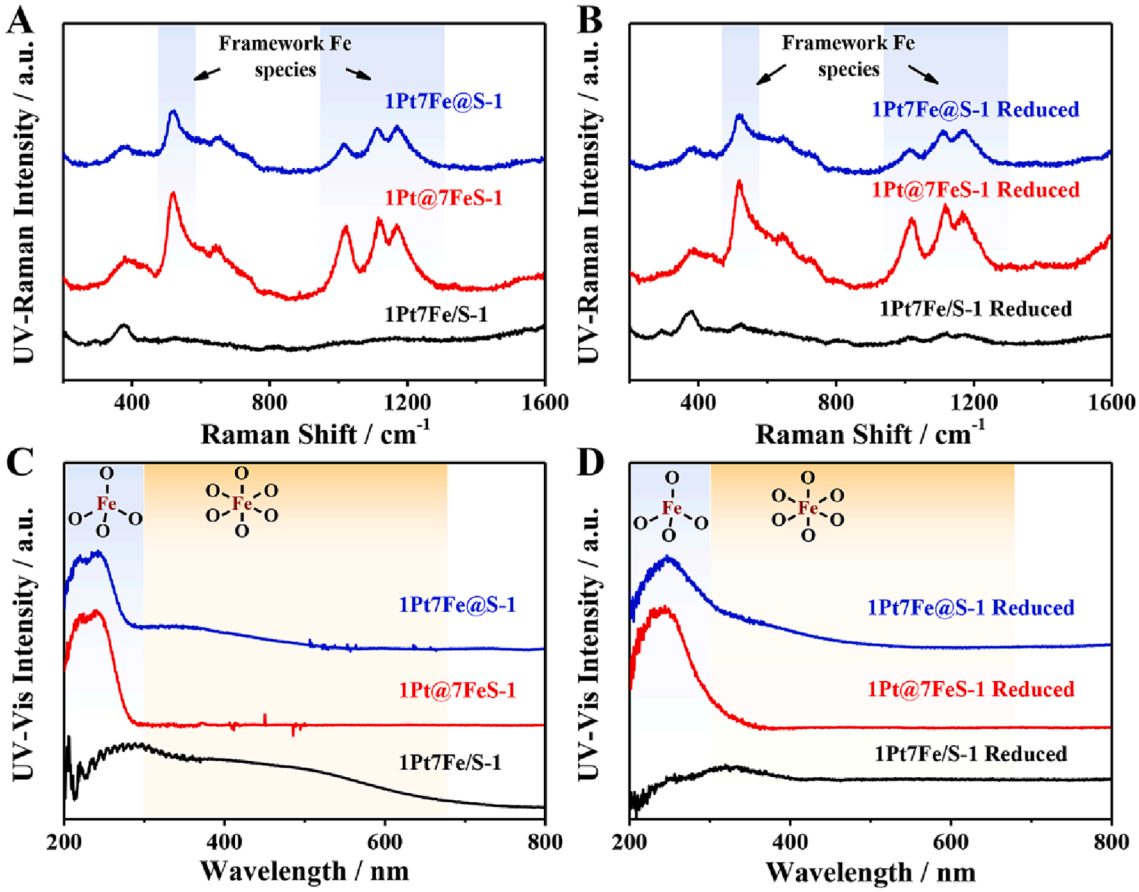

Fig. 1. The UV-Raman (A, B) and UV–Vis (C, D) spectra for three PtFe bimetallic catalysts with different Fe states.

Table 1
The element content of each species in three PtFe bimetallic catalysts with different Fe states.

Element Content	Extra-framework Fe (wt%) [a]	Pt (wt%) [b]	Framework Fe (wt%) [b]
1Pt7Fe/S-1	0.95	0.47	0.01
1Pt@7FeS-1	0.00	0.45	0.96
1Pt7Fe@S-1	0.05	0.46	0.88

[a] Extra-framework Fe content: 10% HNO_3 treatment;
[b] Pt and framework Fe content: HF and aqua regia treatment.

(Fig. 3**A**) spectrum of the reduced 1Pt7Fe/S-1 lies between metallic Fe foil and Fe_2O_3, indicating the presence of both Fe^0 and oxidized Fe species (Bian et al., 2022; He et al., 2023). The reduced 1Pt@7FeS-1 shows a pre-edge feature of Fe^{3+} species and a higher edge energy than metallic Fe^0 species, which conforms with the results of framework Fe species in UV-Raman and UV–Vis. For 1Pt7Fe@S-1, there is a similar pre-edge feature characteristic of Fe^{3+} species, but a lower edge energy was observed, indicating the presence of both framework Fe and metallic Fe^0 species, consistent with the Mössbauer and ICP results. In Fig. 3**B**, the Pt L_{III} edge XANES spectrum of three PtFe bimetallic catalysts are similar to that of the Pt foil, indicating that the Pt species are in the metallic form (Pt^0 in the PtFe alloy) (Wegener et al., 2020). Although the Fe K edge EXAFS spectra are of low quality and do not allow detailed

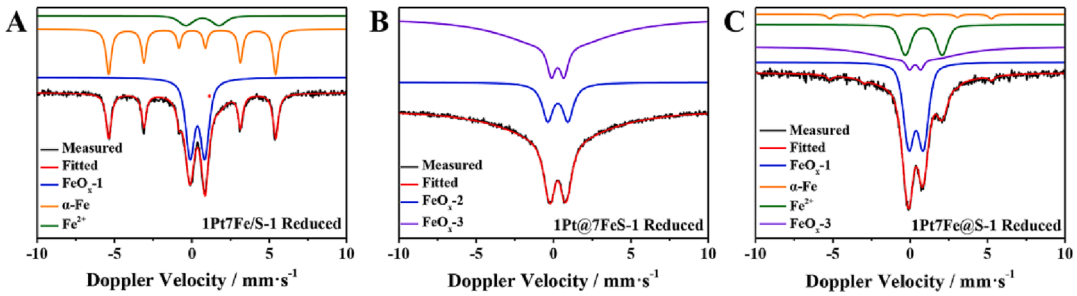

Fig. 2. The Mössbauer spectra for three PtFe bimetallic catalysts with different Fe states after reduction. (A) 1Pt7Fe/S-1; (B) 1Pt@7FeS-1; (C) 1Pt7Fe@S-1.

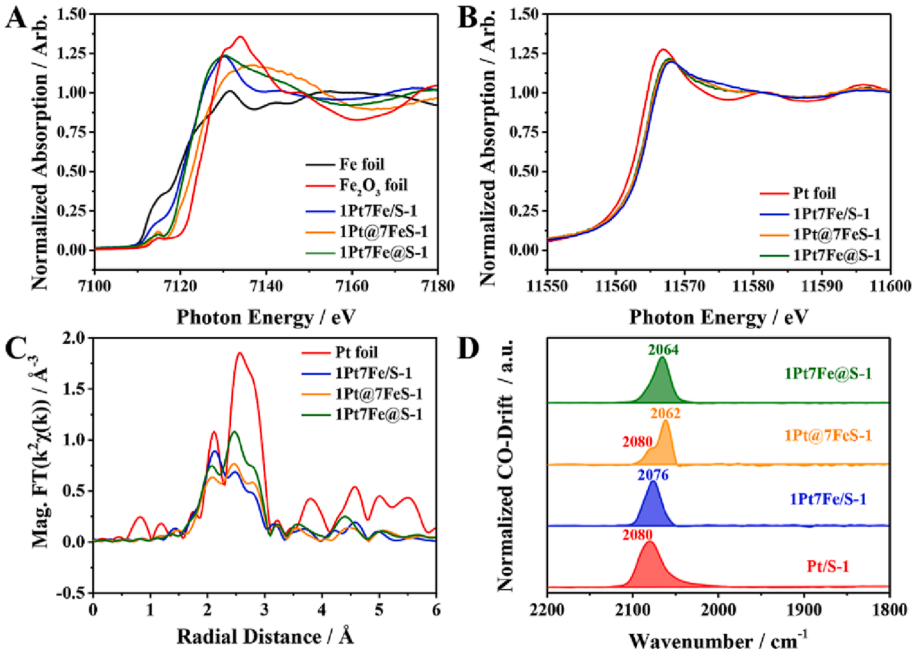

Fig. 3. The *in-situ* XAS: The Fe K edge (A), Pt L_{III} edge (B) XANES spectra, and the magnitude of Fourier Transform of the k^2 weighted Pt L_{III} edge (C) EXAFS spectra; and *in-situ* CO-Drifts results (D) for three PtFe bimetallic catalysts with different states of Fe species.

Table 2
The Pt L_{III} edge XANES and EXAFS fitting parameters for three PtFe bimetallic catalysts with different Fe states after reduction.

Catalyst	Pt L_{III} Edge Energy (eV)	Scattering Pair	S_0^2	CN	R (Å)	σ^2 (Å^2)	ΔE_0 (eV)
Pt foil	11563.5	Pt-Pt	0.85	12 (fixed)	2.77 ± 0.01	0.005 ± 0.001	8.2 ± 0.3
1Pt7Fe7/S-1	11564.5	Pt-Pt		6.7 ± 1.4	2.73 ± 0.01	0.008 ± 0.001	4.4 ± 1.1
		Pt-Fe		1.3 ± 0.6	2.58 ± 0.01	0.006 ± 0.003	
1Pt@7FeS-1	11564.4	Pt-Pt		6.8 ± 1.2	2.73 ± 0.01	0.007 ± 0.001	4.1 ± 1.2
		Pt-Fe		0.9 ± 0.7	2.59 ± 0.03	0.010 ± 0.006	
1Pt7Fe@S-1	11564.4	Pt-Pt		7.2 ± 1.1	2.73 ± 0.01	0.006 ± 0.001	4.5 ± 1.0
		Pt-Fe		1.6 ± 0.9	2.65 ± 0.03	0.014 ± 0.006	

analysis, while the Pt L_{III} edge EXAFS spectra (Fig. 3**C** and Table 2) provided structural information. The wavelet analysis of the Pt L_{III} edge EXAFS is shown in **Fig. S3**. For the Pt foil, the Pt scattering features are centered at R ≈ 2.7 Å and k ≈ 9.5 $Å^{-1}$, whereas for 1Pt7Fe/S-1 the main scattering paths produce features centered at R ≈ 2.2 Å and k ≈ 6.6 $Å^{-1}$. The rise of the contribution at lower k and R indicates the presence of lighter (than Pt) scatterers, and in this case, Fe, within bonding distance surrounding Pt. The scattering features of 1Pt@7FeS-1 and 1Pt7Fe@S-1 are centered at R ≈ 2.4 Å and k ≈ 6.9 $Å^{-1}$, again indicating the presence of Fe scatterers within bonding distance. 1Pt@7FeS-1 has the smallest number of Pt-Fe bonds (2.59 Å with a CN of 0.9 ± 0.7), since most of the Fe species are in the framework of the zeolite. In the *in-situ* CO-Drifts, the Pt/S-1 shows one peak located at 2080 cm^{-1} (Fig. 3**D**), which is usually attributed to the linear-adsorbed CO on terrace Pt sites (Sun et al., 2020). This peak shifts to a lower wavenumber at 2076 cm^{-1} after the introduction of Fe, which indicates the formation of PtFe alloy after H_2 reduction (Bian et al., 2022). The linear CO adsorption peak of 1Pt@7FeS-1 splits into two peaks located at 2062 and 2080 cm^{-1}, and the latter indicates the existence of unalloyed Pt. For 1Pt7Fe@S-1, the peak located at 2080 cm^{-1} disappeared and only one peak at 2064 cm^{-1} was observed, indicating a fully alloyed surface structure (Soares et al., 2016; Zhang et al., 2016). These results demonstrate that the structures of Pt species among three PtFe bimetallic catalysts are influenced by tuning the states of Fe species.

The distribution of metallic species among three PtFe bimetallic catalysts was also investigated. As shown in the XRD results in **Fig. S4A**, only the diffraction peaks of the typical MFI topology were observed for all three catalysts, without any observable diffraction peaks from metal species, indicating that the metal species are all well dispersed. Fig. 4 **and S5** provide the HR-TEM, HADDF-STEM and EDS mapping images for three PtFe bimetallic catalysts after reduction, respectively. Uniform zeolite crystal size with a diameter of about 200 nm was observed for all samples, which agrees with the typical MFI topology diffraction peaks in **Fig. S4A** (Han et al., 2022; Yang et al., 2017). Large amounts of metal nanoparticles with an average size of 3.3 nm are on the surface of the zeolite crystals in the reduced 1Pt7Fe/S-1, as shown in Fig. 4 **and S5**, and a lattice spacing of 2.23 Å was observed, suggesting the presence of the Pt_3Fe_1 alloy phase after H_2 reduction (PDF#89–2050). On the contrary, large amounts of highly-dispersed metal nanoparticles with an average size of 1.5 nm are encapsulated inside the zeolite crystals in the reduced 1Pt@7FeS-1 and 1Pt7Fe@S-1, which is well supported by the near zero activity for the hydrogenation of 3-Nitrotoluene with $NaBH_4$, as shown in **Fig. S6** (Huang et al., 2023; Sun et al., 2019).

3.2. Catalytic performance

Fig. 5 shows the catalytic performance of the monometallic Pt and the three PtFe bimetallic catalysts with different Fe states, and the TGA results of each spent catalyst are displayed in Fig. 5**D**. Due to the monometallic FeS-1 (framework Fe species) and Fe/S-1 (extra-framework Fe species) show less than 1% of C_3H_8 conversion, as shown in **Fig. S7**, thus their contributions in PDH are negligible. The monometallic Pt/S-1 shows a poor PDH activity and stability. The initial C_3H_8 conversion was 37% and rapidly decreased to 2% in 280 min. Although the Pt@S-1 has higher initial C_3H_8 conversion (49%), a comparable deactivation trend with Pt/S-1 and lower initial C_3H_6 selectivity of 82% were observed. Both of the monometallic Pt catalysts produced about 2.0 wt% of coke after 280 min on stream. The initial activity and stability increase dramatically after introducing 1.0 wt% of Fe species. The C_3H_8 conversion of 1Pt7Fe/S-1 increased to 58% and stabilized at 53% after 280 min. The initial C_3H_6 selectivity was 73%, and increased above 92% within 60 min. The carbon balance was 81% at the initial stage, and increased to 92% with progress of the reaction. The TGA result shows that the 1Pt7Fe/S-1 produces about 15.4 wt% of coke after 280 min on stream. In addition, the TEM images (**Fig. S8**) and the more intense carbon signal located at 1335 and 1602 cm^{-1} in Vis-Raman spectra (**Fig. S9**) also confirm the presence of more amorphous coke on the surface of spent 1Pt7Fe/S-1 (Sattler et al., 2014a). In contrast,

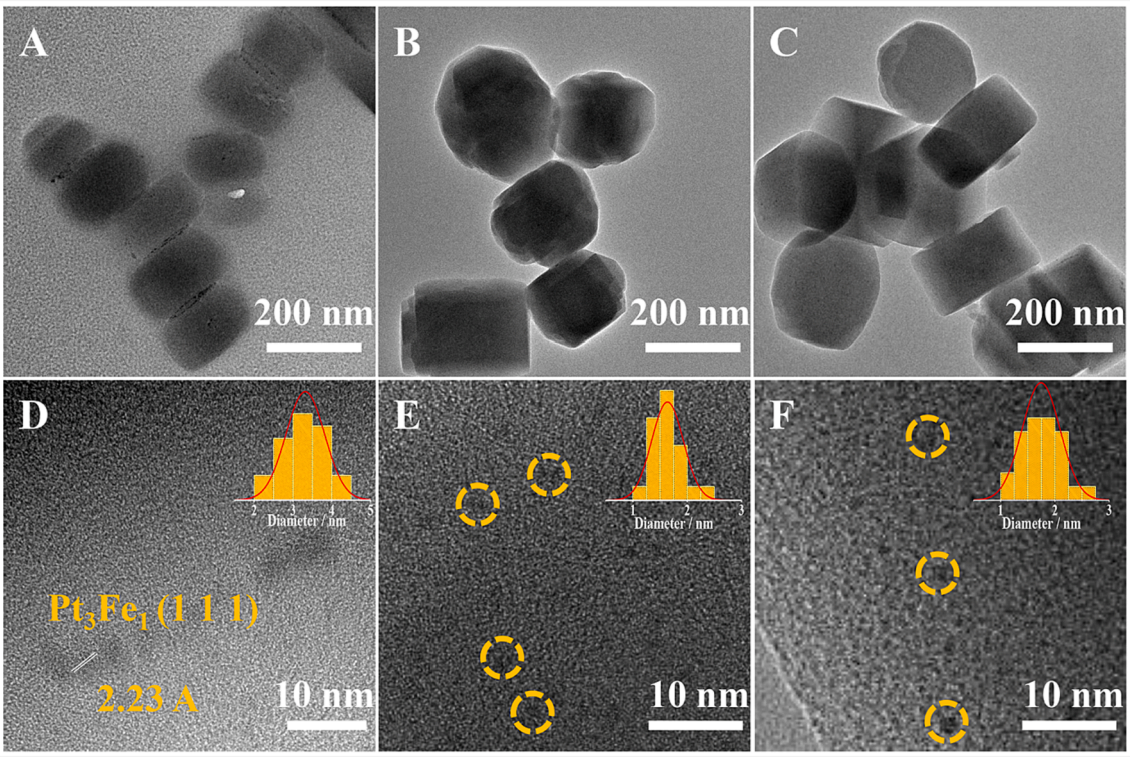

Fig. 4. The TEM and HR-TEM images for three PtFe bimetallic catalysts with different states of Fe species after reduction. (A, D) 1Pt7Fe/S-1; (B, E) 1Pt@7FeS-1; and (C, F) 1Pt7Fe@S-1.

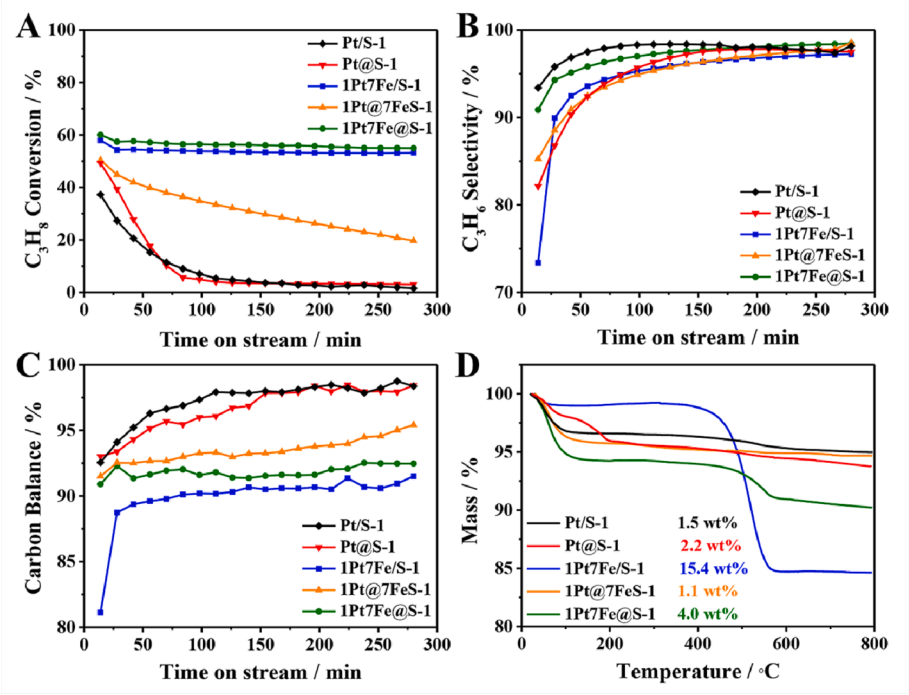

Fig. 5. The catalytic performance for monometallic Pt and three PtFe bimetallic catalysts with different Fe states. (A) The C_3H_8 conversion; (B) The C_3H_6 selectivity; (C) The C_3H_8 carbon balance; (D) The TGA results for the spent catalysts after 280 min on stream. Reaction conditions: T = 550 ℃, ambient pressure, 0.15 g of the catalyst, C_3H_8/N_2 = 5/35 mL/min, GHSV = 16000 mL·h^{-1}·g$_{cat}^{-1}$.

1Pt@7FeS-1 only produced 1.1 wt% of coke, the stability is noticeably worse compared to the 1Pt7Fe/S-1 catalyst. The initial C_3H_8 conversion was 50% and decreased to 20% after 280 min. The initial C_3H_6 selectivity and carbon balance reached 85% and 91%, respectively. It should be noted that the 1Pt7Fe@S-1 achieved the best catalytic performance among three PtFe bimetallic catalysts. The initial C_3H_8 conversion reaches 60% and stabilizes at 55% in 280 min. The carbon balance and initial selectivity of propylene are both above 91%, and the latter gradually increases to 98% after 280 min on stream. In addition, the TGA results and TEM images both show that the spent 1Pt7Fe@S-1 only produces about 4.0 wt% of coke, much less than 1Pt7Fe/S-1 (15.4 wt%).

To ascertain differences in catalytic performance among three PtFe bimetallic catalysts, Fe-2p and Pt-4f XPS were used to characterize three PtFe bimetallic catalysts after PDH reaction. The spent 1Pt7Fe/S-1 shows two peaks located at 707.7 and 711.8 eV after deconvolution in Fe $2p_{3/2}$ range (Fig. 6**A**), which are attributed to metallic Fe and Fe^{3+} species, respectively (Ji et al., 2020; Yuan et al., 2021; Zhang et al., 2018b; Zhu et al., 2020). For the spent 1Pt@7FeS-1 and 1Pt7Fe@S-1, a majority signal of Fe^{3+} species at 711.8 eV was observed. Since the metallic Fe species having a stronger coking and C–C bond breaking ability than FeO_x and PtFe alloy (Wang et al., 2022a; Yang et al., 2020), besides the metallic Fe species transforms into FeC_x with a weaker ability on cracking during the reaction, a lower initial C_3H_6 selectivity and much coke are obtained on the 1Pt7Fe/S-1, which well conforms with the TGA and Mössbauer results. While the Fe species in spent 1Pt@7FeS-1 and 1Pt7Fe@S-1 mainly exist as Fe^{3+} in the framework and remains stable, which effectively eliminates the excess unalloyed metallic Fe^0 species and greatly inhibits the formation of carbon deposition. In addition, the formation of PtFe alloy in 1Pt7Fe/S-1 and 1Pt7Fe@S-1 show high stability in steady state, which indicates that the well-defined PtFe alloy is the major active phase for PDH reaction. While the Fe species in 1Pt@7FeS-1 tends to integrate into the framework of zeolite, rather than stays extra-framework, the insufficient PtFe alloy finally leads to the poor stability and C_3H_6 selectivity, which is supported by the *in-situ* XAS and CO-Drifts. Because the excess Fe species are incorporated into the zeolite framework, the remaining extra-framework Fe and Pt species form well-defined and uniform PtFe alloy nanoparticles. Thus, the 1Pt7Fe@S-1 achieves excellent PDH catalytic performance and greatly inhibits the formation of coke among three PtFe bimetallic catalysts with different Fe states.

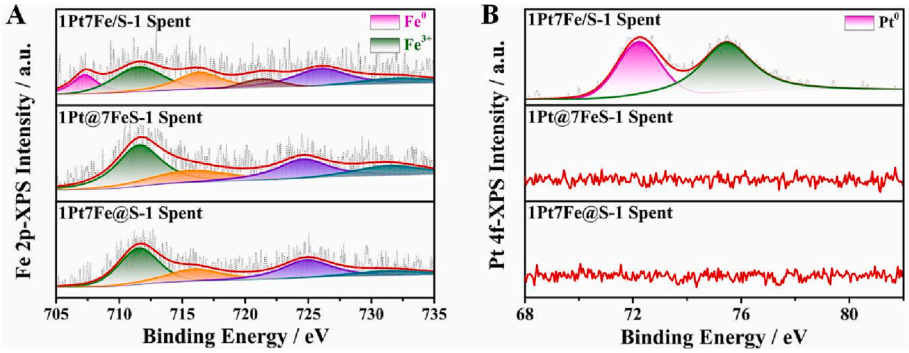

Fig. 6. The Fe-2p (A) and Pt-4f (B) XPS results for three PtFe bimetallic catalysts with different Fe states after PDH reaction.

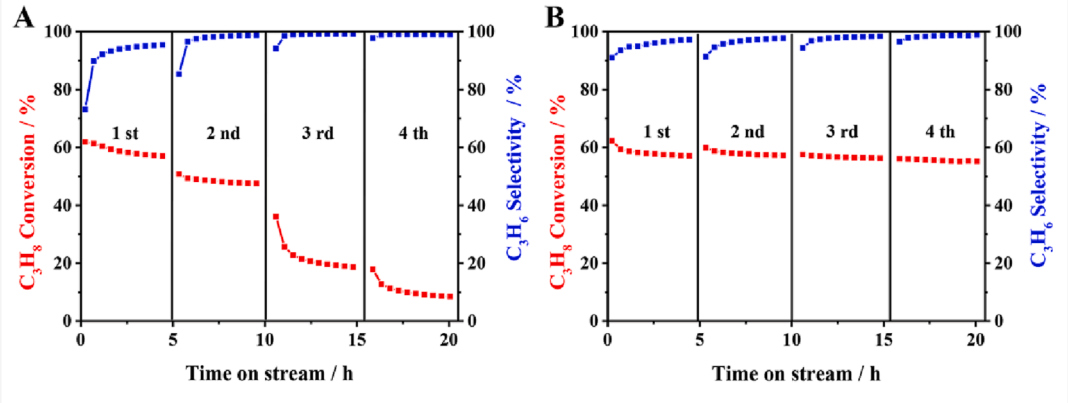

Fig. 7. The catalytic performance on 1Pt7Fe/S-1 (A) and 1Pt7Fe@S-1 (B) catalysts during the successive oxidation–reduction PDH tests. Reaction conditions: T = 550 ℃, ambient pressure, 0.15 g of the catalyst, C_3H_8/N_2 = 5/35 mL/min, GHSV = 16000 mL·h^{-1}·g$_{cat}^{-1}$. Each cycle includes a step of PDH for 5 h, followed by a treatment in air (30 mL/min) at 550 ℃ for 0.85 h to remove the deposited coke and then reduced via pure H_2 (30 mL/min) at 550 ℃ for 0.5 h.

The regeneration stability of 1Pt7Fe/S-1 and 1Pt7Fe@S-1 was investigated by successive oxidation–reduction PDH cycles, and the results are shown in Fig. 7. The initial C_3H_8 conversion and C_3H_6 selectivity of fresh 1Pt7Fe/S-1 reach 62% and 73%, respectively. Across multiple regeneration cycles, the initial propane conversion and stability of 1Pt7Fe/S-1 gradually decrease and show an irreversible deactivation during each regeneration. The initial C_3H_8 conversion dramatically decreases to 18% in the fourth cycle. In contrast, the initial activity and C_3H_6 selectivity of fresh 1Pt7Fe@S-1 are 62% and 91%, respectively. After four cycles, the initial C_3H_8 conversion of 1Pt7Fe@S-1 remains high at 56%, and the C_3H_6 selectivity stabilizes above 97%, similar to the fresh catalyst. Combined with the TEM results (Fig. 4) and absent signal of Pt 4f-XPS (Fig. 6**B**), the well-defined PtFe alloy in 1Pt7Fe@S-1 are encapsulated at the interior of the zeolite, which significantly improves the anti-sintering ability of metal particles, thus showing the excellent recycling stability during the successive oxidation–reduction PDH test (Sun et al., 2020; Wang et al., 2020).

3.3. Structure and performance optimization

To further optimize the structure and its PDH catalytic performance, a series of PtFe@S-1 bimetallic catalysts with similar nanoparticle sizes (**Fig. S10**) but different Pt/Fe molar ratios were prepared and tested in Fig. 8, and the relevant results of UV–Vis spectra and *in-situ* CO-Drifts are shown in Fig. 9. The initial C_3H_8 conversion of 3Pt1Fe@S-1 is 46 % and decreases to 5% within 280 min, which shows a similar deactivation trend to the Pt@S-1. The initial C_3H_6 selectivity and carbon balance reach 91% and 94%, respectively. The TGA result shows that it produces 1.1 wt% of coke after reaction. As observed in the UV–Vis spectra, the Fe species mainly integrates into the framework of zeolite with a low Fe content in Fig. 9**A**. Meanwhile, a signal of CO linearly adsorbed on Pt (2080 cm^{-1}) is observed on 3Pt1Fe@S-1 in Fig. 9**B**, which indicates that the incomplete PtFe alloying on the surface leads to a poor stability and low initial activity. While the activity and stability significantly increase with increased Fe content. The C_3H_8 conversion of 1Pt1Fe@S-1 reaches

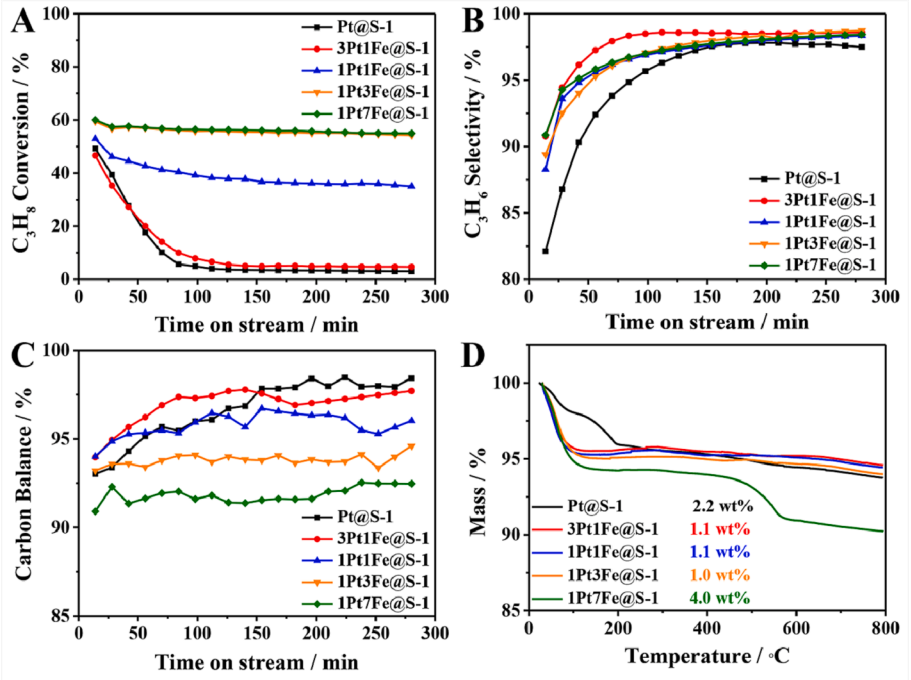

Fig. 8. The catalytic performance for PtFe@S-1 catalysts with different Pt/Fe molar ratio after 280 min on stream. (A) The C_3H_8 conversion; (B) The C_3H_6 selectivity; (C) The C_3H_8 carbon balance; (D) The TGA results for the spent catalysts after 280 min on stream. Reaction conditions: T = 550 ℃, ambient pressure, 0.15 g of the catalyst, C_3H_8/N_2 = 5/35 mL/min, GHSV = 16000 mL·h^{-1}·g$_{cat}^{-1}$.

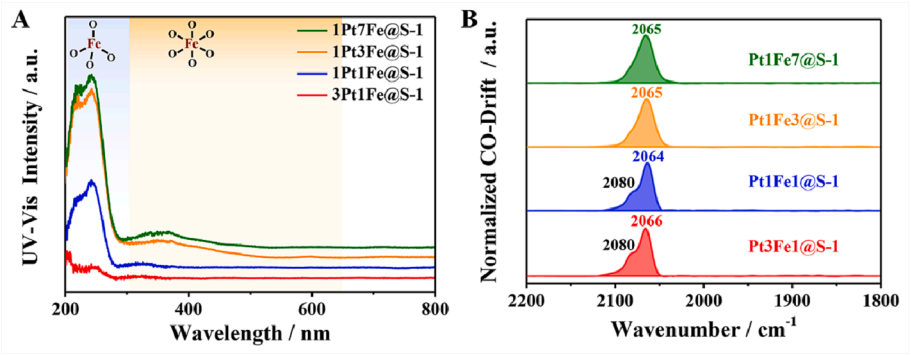

Fig. 9. The UV–Vis spectra (A) and *in-situ* CO-Drifts (B) for PtFe@S-1 catalysts with different Pt/Fe molar ratio.

53% and decreases to 35% in 280 min. The carbon balance reaches 94% and gradually increases to 96%. In addition, it shows a similar C_3H_6 selectivity and coke amount (1.1 wt%) with 3Pt1Fe@S-1. When the Pt/Fe ratio decreases to 1:3, more extra-framework Fe species appears in Fig. 9**A**. At the same time, the signal of CO linearly adsorbed on Pt (2080 cm^{-1}) disappears in Fig. 9**B**, indicating the formation of PtFe alloy in 1Pt3Fe@S-1, which is related with the significantly enhanced catalytic performance in Fig. 8. The C_3H_8 conversion further increases to 59% and stabilizes at 54% after 280 min. The initial C_3H_6 selectivity reaches 90% and gradually improves to 99%. The carbon balance is above 93%, and 1.0 wt% of coke is produced after 280 min on stream. Further increasing the nominal Fe content, the catalytic performance of 1Pt7Fe@S-1 is similar with that of 1Pt3Fe@S-1. However, due to the presence of less unalloyed Fe species (3.3%, from the results of Mössbauer spectrum), its carbon deposition slightly increases to 4.0 wt%.

The long-term stability test for PDH reaction over 1Pt3Fe@S-1 was investigated in Fig. 10. After 50 h on stream, the propane conversion remains at 42% with a low deactivation constant of 0.010 h^{-1}. The propylene selectivity maintains above 99% and forms 2.8 wt% of coke in TGA results. In addition, the 1Pt3Fe@S-1 shows a high TOF of C_3H_6 in **Fig. S11**, reaching 8.2 s^{-1}. Therefore, the optimized catalytic structure is achieved with 1Pt3Fe@S-1, which displays the best catalytic performance and less coke among various nominal Pt/Fe ratio samples.

4. Conclusion

In this manuscript, we offer an effective strategy to obtain optimized catalytic structure and PDH catalytic performance by integrating excess unalloyed metallic Fe into the FeO_x species in the zeolite framework meanwhile obtaining well-defined and uniform PtFe alloy nanoparticles. Excessive unalloyed Fe^0 species produces much coke in PDH reaction. When the Fe species completely integrates into the framework of the zeolite, it produces less carbon, but the incomplete PtFe alloying on the surface leads to a poor propylene selectivity and rapid deactivation. Due to the unique structure of 1Pt3Fe@S-1, most of the Fe species integrates into the framework of zeolite, which effectively eliminates the excess unalloyed metallic Fe^0 species and greatly inhibits the formation of carbon deposition. Meanwhile, the remainder of extra-framework Fe and Pt species encapsulated in the channel of zeolite form well-defined PtFe alloy nanoparticles, which significantly improves the C_3H_6 selectivity and catalytic stability. This work provides insight into the structure–activity relationship of the PDH reaction, and will advance future structural design and optimization of PtFe bimetallic catalysts.

Data availability

Data will be made available on request.

CRediT authorship contribution statement

Kai Bian: Investigation, Methodology, Writing – review & editing, Visualization. **Guanghui Zhang:** Conceptualization, Funding acquisition, Formal analysis, Supervision, Writing – review & editing. **Mingrui Wang:** Methodology, Formal analysis, Visualization. **Shida Liu:** Investigation, Methodology. **Christian J. Breckner:** Methodology, Formal analysis. **David P. Dean:** Methodology, Formal analysis. **Jie Zhu:** Investigation, Methodology. **Jeffrey T. Miller:** Methodology, Writing – review & editing. **Shuandi Hou:** Conceptualization, Supervision,

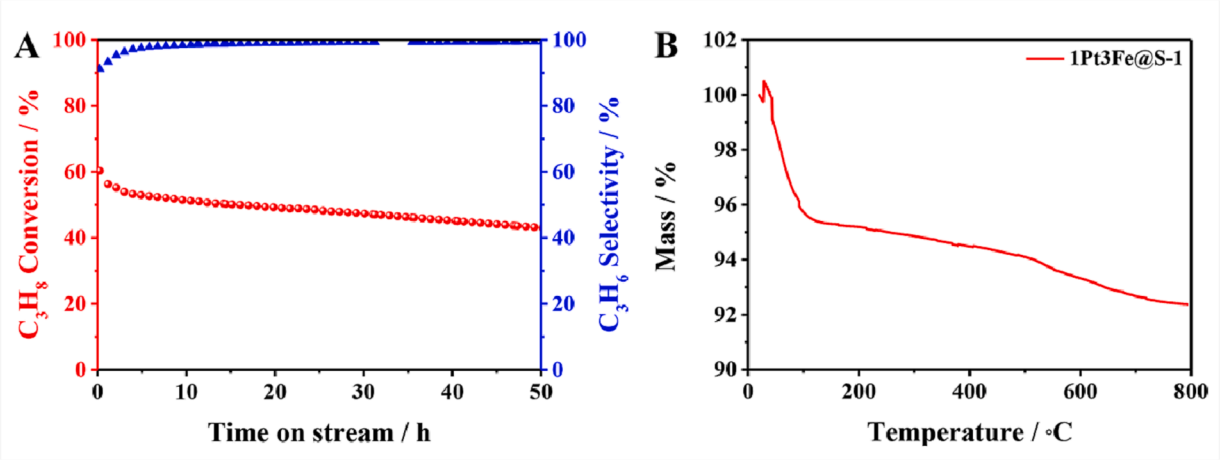

Fig. 10. The long-term stability test (A) and the TG results (B) for PDH reaction over 1Pt3Fe@S-1. Reaction conditions: T = 550 ℃, ambient pressure, 0.15 g of the catalyst, C_3H_8/N_2 = 5/35 mL/min, GHSV = 16000 mL·h^{-1}·g_{cat}^{-1}.

Writing – review & editing. **Chunshan Song:** Conceptualization, Supervision, Writing – review & editing. **Xinwen Guo:** Conceptualization, Supervision, Writing – review & editing, Funding acquisition.

Declaration of Competing Interest

The authors declare that they have no known competing financial interests or personal relationships that could have appeared to influence the work reported in this paper.

Data availability

Data will be made available on request.

Acknowledgments

This work was financially supported by the National Natural Science Foundation of China (21902019), the Liaoning Revitalization Talent Program (XLYC2008032), the CUHK Research Startup Fund (No. #4930981), and the Fundamental Research Funds for the Central Universities (DUT22LK24, DUT22LAB602, and DUT22QN207). CJB, DPD and JTM were funded by the National Science Foundation under Cooperative Agreement No. EEC-1647722 (CISTAR – NSF Engineering Research Center for Innovative and Strategic Transformation of Alkane Resources). Use of the Advanced Photon Source was supported by the U. S. Department of Energy under Contract No. DE-AC02-06CH11357. MRCAT operations and the beamline 10-BM were supported by the Department of Energy and the MRCAT member institutions. We acknowledge the Center for Advanced Mössbauer Spectroscopy, Mössbauer Effect Data Center, Dalian Institute of Chemical Physics, CAS, for providing the Mössbauer measurement and analysis.

Appendix A. Supplementary data

Supplementary data to this article can be found online at https://doi.org/10.1016/j.ces.2023.118748.

References

Atanga, M.A., Rezaei, F., Jawad, A., Fitch, M., Rownaghi, A.A., 2018. Oxidative dehydrogenation of propane to propylene with carbon dioxide. Appl. Catal. B-Environ. 220, 429–445.

Bian, K., Zhang, G., Zhu, J., Wang, X., Wang, M., Lou, F., Liu, Y., Song, C., Guo, X., 2022. Promoting Propane Dehydrogenation with CO_2 over the PtFe Bimetallic Catalyst by Eliminating the Non-selective Fe(0) Phase. ACS Catal. 12, 6559–6569.

Cai, W., Mu, R., Zha, S., Sun, G., Chen, S., Zhao, Z.J., Li, H., Tian, H., Tang, Y., Tao, F.F., Zeng, L., Gong, J., 2018. Subsurface catalysis-mediated selectivity of dehydrogenation reaction. Sci. Adv. 4, eaar5418.

Carter, J.H., Bere, T., Pitchers, J.R., Hewes, D.G., Vandegehuchte, B.D., Kiely, C.J., Taylor, S.H., Hutchings, G.J., 2021. Direct and oxidative dehydrogenation of propane: from catalyst design to industrial application. Green Chem. 23, 9747–9799.

Cesar, L.G., Yang, C., Lu, Z., Ren, Y., Zhang, G., Miller, J.T., 2019. Identification of a Pt_3Co Surface Intermetallic Alloy in Pt–Co Propane Dehydrogenation Catalysts. ACS Catal. 9, 5231–5244.

Chen, S., Pei, C., Sun, G., Zhao, Z.-J., Gong, J., 2020. Nanostructured Catalysts toward Efficient Propane Dehydrogenation. Acc. Mater. Res. 1, 30–40.

Chen, S., Chang, X., Sun, G., Zhang, T., Xu, Y., Wang, Y., Pei, C., Gong, J., 2021a. Propane dehydrogenation: catalyst development, new chemistry, and emerging technologies. Chem. Soc. Rev. 50, 3315–3354.

Chen, X., Peng, M., Cai, X., Chen, Y., Jia, Z., Deng, Y., Mei, B., Jiang, Z., Xiao, D., Wen, X., Wang, N., Liu, H., Ma, D., 2021c. Regulating coordination number in atomically dispersed Pt species on defect-rich graphene for n-butane dehydrogenation reaction. Nat. Commun. 12, 2664.

Chen, S., Zhao, Z.-J., Mu, R., Chang, X., Luo, J., Purdy, S.C., Kropf, A.J., Sun, G., Pei, C., Miller, J.T., Zhou, X., Vovk, E., Yang, Y., Gong, J., 2021b. Propane Dehydrogenation on Single-Site $[PtZn_4]$ Intermetallic Catalysts. Chem. 7, 387–405.

Cybulskis, V.J., Bukowski, B.C., Tseng, H.-T., Gallagher, J.R., Wu, Z., Wegener, E., Kropf, A.J., Ravel, B., Ribeiro, F.H., Greeley, J., Miller, J.T., 2017. Zinc Promotion of Platinum for Catalytic Light Alkane Dehydrogenation: Insights into Geometric and Electronic Effects. ACS Catal. 7, 4173–4181.

Dai, Y., Gao, X., Wang, Q., Wan, X., Zhou, C., Yang, Y., 2021a. Recent progress in heterogeneous metal and metal oxide catalysts for direct dehydrogenation of ethane and propane. Chem. Soc. Rev. 50, 5590–5630.

Dai, Y., Wu, Y., Dai, H., Gao, X., Tian, S., Gu, J., Yi, X., Zheng, A., Yang, Y., 2021b. Effect of coking and propylene adsorption on enhanced stability for Co^{2+}-catalyzed propane dehydrogenation. J. Catal. 395, 105–116.

Dai, C., Zhang, A., Liu, M., Guo, X., Song, C., 2015. Hollow ZSM-5 with Silicon-Rich Surface, Double Shells, and Functionalized Interior with Metallic Nanoparticles and Carbon Nanotubes. Adv. Fun. Mater. 25, 7479–7487.

Dai, C., Zhang, A., Liu, M., Gu, L., Guo, X., Song, C., 2016. Hollow Alveolus-Like Nanovesicle Assembly with Metal-Encapsulated Hollow Zeolite Nanocrystals. ACS Nano 10, 7401–7408.

Escorcia, N.J., LiBretto, N.J., Miller, J.T., Li, C.W., 2020. Colloidal Synthesis of Well-Defined Bimetallic Nanoparticles for Nonoxidative Alkane Dehydrogenation. ACS Catal. 10, 9813–9823.

Estes, D.P., Siddiqi, G., Allouche, F., Kovtunov, K.V., Safonova, O.V., Trigub, A.L., Koptyug, I.V., Coperet, C., 2016. C-H Activation on Co, O Sites: Isolated Surface Sites versus Molecular Analogs. J. Am. Chem. Soc. 138, 14987–14997.

Fan, X., Liu, D., Sun, X., Yu, X., Li, D., Yang, Y., Liu, H., Diao, J., Xie, Z., Kong, L., Xiao, X., Zhao, Z., 2020. Mn-doping induced changes in Pt dispersion and Pt_xMn_y alloying extent on Pt/Mn-DMSN catalyst with enhanced propane dehydrogenation stability. J. Catal. 389, 450–460.

Fan, F., Sun, K., Feng, Z., Xia, H., Han, B., Lian, Y., Ying, P., Li, C., 2009. From molecular fragments to crystals: a UV Raman spectroscopic study on the mechanism of Fe-ZSM-5 synthesis. Chem. 15, 3268–3276.

Fierro, G., Moretti, G., Ferraris, G., Andreozzi, G.B., 2011. A Mössbauer and structural investigation of Fe-ZSM-5 catalysts: Influence of Fe oxide nanoparticles size on the catalytic behaviour for the NO-SCR by C_3H_8. Appl. Catal. B-Environ. 102, 215–223.

Han, Z., Li, S., Jiang, F., Wang, T., Ma, X., Gong, J., 2014. Propane dehydrogenation over Pt-Cu bimetallic catalysts: the nature of coke deposition and the role of copper. Nanoscale 6, 10000–10008.

Han, H., Zhang, A., Ren, L., Nie, X., Liu, M., Liu, Y., Shi, C., Yang, H., Song, C., Guo, X., 2022. Coke-resistant (Pt + Ni)/ZSM-5 catalyst for shape-selective alkylation of toluene with methanol to para-xylene. Chem. Eng. Sci. 252, 117529.

He, X., Gao, X., Chen, X., Hu, S., Tan, F., Xiong, Y., Long, R., Liu, M., Tse, E.C.M., Wei, F., Yang, H., Hou, J., Song, C., Guo, X., 2023. Dual-optimization strategy engineered Ti-based metal-organic framework with Fe active sites for highly-selective CO_2 photoreduction to formic acid. Appl. Catal. B-Environ. 327, 122418.

Hu, Z.P., Qin, G., Han, J., Zhang, W., Wang, N., Zheng, Y., Jiang, Q., Ji, T., Yuan, Z.Y., Xiao, J., Wei, Y., Liu, Z., 2022. Atomic Insight into the Local Structure and Microenvironment of Isolated Co-Motifs in MFI Zeolite Frameworks for Propane Dehydrogenation. J. Am. Chem. Soc. 144, 12127–12137.

Hu, B., Schweitzer, N.M., Zhang, G., Kraft, S.J., Childers, D.J., Lanci, M.P., Miller, J.T., Hock, A.S., 2015. Isolated Fe^{II} on Silica As a Selective Propane Dehydrogenation Catalyst. ACS Catal. 5, 3494–3503.

Huang, H., Fan, H., Ge, Y., Ye, W., Liu, Y., Song, C., Lin, H., Zhang, X., Li, B., Nie, X., Zhang, S., Lu, R., 2023. Solvent-free oxidation of toluene to benzaldehyde using electron-rich Au clusters confined in Silicalite-1. Chem. Eng. J. 458, 141446.

Ji, L., Peng, X., Wang, Z., 2020. Oxygen Vacancy-Enriched FeO_x Nanoparticle Electrocatalyst for the Oxygen Reduction Reaction. Trans. Tianjin Univ. 26, 373–381.

Lari, G.M., Mondelli, C., Pérez-Ramírez, J.,, 2015. Gas-Phase Oxidation of Glycerol to Dihydroxyacetone over Tailored Iron Zeolites. ACS Catal. 5, 1453–1461.

Li, Y., Li, J., Yang, X., Wang, X., Xu, Y., Zhang, L., 2018. Preparation of CeO_2-Modified Mg(Al)O-Supported Pt–Cu Alloy Catalysts Derived from Hydrotalcite-Like Precursors and Their Catalytic Behavior for Direct Dehydrogenation of Propane. Trans. Tianjin Univ. 25, 169–184.

LiBretto, N.J., Yang, C., Ren, Y., Zhang, G., Miller, J.T., 2019. Identification of Surface Structures in Pt_3Cr Intermetallic Nanocatalysts. Chem. Mater. 31, 1597–1609.

Liu, H., Dong, X., Xia, J., Li, X., Sun, Y., Cai, Q., 2019a. Preparation of γ-Al_2O_3 via Hydrothermal Synthesis Using ρ-Al_2O_3 as Raw Material for Propane Dehydrogenation. Trans. Tianjin Univ. 26, 362–372.

Liu, L., Lopez-Haro, M., Lopes, C.W., Li, C., Concepcion, P., Simonelli, L., Calvino, J.J., Corma, A., 2019b. Regioselective generation and reactivity control of subnanometric platinum clusters in zeolites for high-temperature catalysis. Nat. Mater. 18, 866–873.

Liu, S., Zhang, B., Liu, G., 2021. Metal-based catalysts for the non-oxidative dehydrogenation of light alkanes to light olefins. React. Chem. Eng. 6, 9–26.

Liu, Y., Zhang, G., Liu, S., Zhu, J., Liu, J., Wang, J., Li, R., Wang, M., Fu, Q., Hou, S., Song, C., Guo, X., 2022. Promoting n-Butane Dehydrogenation over $PtMn/SiO_2$ through Structural Evolution Induced by a Reverse Water-Gas Shift Reaction. ACS Catal. 12, 13506–13512.

Liu, H., Zhou, J., Chen, T., Hu, P., Xiong, C., Sun, Q., Chen, S., Lo, T.W.B., Ji, H., 2023. Isolated Pt Species Anchored by Hierarchical-like Heteroatomic Fe-Silicalite-1 Catalyze Propane Dehydrogenation near the Thermodynamic Limit. ACS Catal. 13, 2928–2936.

Lobera, M.P., Biausque, G., Téllez, C., Herguido, J., Menéndez, M., Schuurman, Y., 2010. Comparison of different methods for quantitative analysis of TAP pulse-response data for propane dehydrogenation over Pt–Sn–K/γ–Al_2O_3. Chem. Eng. Sci. 65, 2417–2424.

Luo, L., Dai, C., Zhang, A., Wang, J., Song, C., Guo, X., 2016. Evolution of iron species for promoting the catalytic performance of FeZSM-5 in phenol oxidation. RSC Adv. 6, 32789–32797.

Nakaya, Y., Xing, F., Ham, H., Shimizu, K.I., Furukawa, S., 2021. Doubly Decorated Platinum-Gallium Intermetallics as Stable Catalysts for Propane Dehydrogenation. Angew. Chem. Int. Ed. 60, 19715–19719.

Pérez-Ramírez, J., Gallardo-Llamas, A., Daniel, C., Mirodatos, C., 2004. N_2O-mediated propane oxidative dehydrogenation over Fe-zeolites. TEOM studies for continuous propylene production in a cyclically-operated reactor. Chem. Eng. Sci. 59, 5535–5543.

Purdy, S.C., Ghanekar, P., Mitchell, G., Kropf, A.J., Zemlyanov, D.Y., Ren, Y., Ribeiro, F., Delgass, W.N., Greeley, J., Miller, J.T., 2020. Origin of Electronic Modification of Platinum in a Pt_3V Alloy and Its Consequences for Propane Dehydrogenation Catalysis. ACS Appl. Energy Mater. 3, 1410–1422.

Rochlitz, L., Searles, K., Alfke, J., Zemlyanov, D., Safonova, O.V., Coperet, C., 2019. Silica-supported, narrowly distributed, subnanometric Pt-Zn particles from single sites with high propane dehydrogenation performance. Chem. Sci. 11, 1549–1555.

Rochlitz, L., Pessemesse, Q., Fischer, J.W.A., Klose, D., Clark, A.H., Plodinec, M., Jeschke, G., Payard, P.A., Coperet, C., 2022. A Robust and Efficient Propane Dehydrogenation Catalyst from Unexpectedly Segregated Pt_2Mn Nanoparticles. J. Am. Chem. Soc. 144, 13384–13393.

Sattler, J.J., Gonzalez-Jimenez, I.D., Luo, L., Stears, B.A., Malek, A., Barton, D.G., Kilos, B.A., Kaminsky, M.P., Verhoeven, T.W., Koers, E.J., Baldus, M., Weckhuysen, B.M., 2014a. Platinum-promoted Ga/Al_2O_3 as highly active, selective, and stable catalyst for the dehydrogenation of propane. Angew. Chem. Int. Ed. 53, 9251–9256.

Sattler, J.J., Ruiz-Martinez, J., Santillan-Jimenez, E., Weckhuysen, B.M., 2014b. Catalytic dehydrogenation of light alkanes on metals and metal oxides. Chem. Rev. 114, 10613–10653.

Searles, K., Chan, K.W., Mendes Burak, J.A., Zemlyanov, D., Safonova, O., Coperet, C., 2018. Highly Productive Propane Dehydrogenation Catalyst Using Silica-Supported Ga-Pt Nanoparticles Generated from Single-Sites. J. Am. Chem. Soc. 140, 11674–11679.

Shi, L., Deng, G.M., Li, W.C., Miao, S., Wang, Q.N., Zhang, W.P., Lu, A.H., 2015. Al_2O_3 Nanosheets Rich in Pentacoordinate Al^{3+} Ions Stabilize Pt-Sn Clusters for Propane Dehydrogenation. Angew. Chem. Int. Ed. 54, 13994–13998.

Soares, A.-V.-H., Perez, G., Passos, F.B., 2016. Alumina supported bimetallic Pt–Fe catalysts applied to glycerol hydrogenolysis and aqueous phase reforming. Appl. Catal. B-Environ. 185, 77–87.

Sripinun, S., Lorattanaprasert, K., Gayapan, K., Suriye, K., Wannakao, S., Praserthdam, P., Assabumrungrat, S., 2021. Design of hybrid pellet catalysts of WO_3/Si-Al and PtIn/hydrotalcite via dehydrogenation and metathesis reactions for production of olefins from propane. Chem. Eng. Sci. 229, 116025.

Sun, Q., Wang, N., Zhang, T., Bai, R., Mayoral, A., Zhang, P., Zhang, Q., Terasaki, O., Yu, J., 2019. Zeolite-Encaged Single-Atom Rhodium Catalysts: Highly-Efficient Hydrogen Generation and Shape-Selective Tandem Hydrogenation of Nitroarenes. Angew. Chem. Int. Ed. 58, 18570–18576.

Sun, Q., Wang, N., Fan, Q., Zeng, L., Mayoral, A., Miao, S., Yang, R., Jiang, Z., Zhou, W., Zhang, J., Zhang, T., Xu, J., Zhang, P., Cheng, J., Yang, D.C., Jia, R., Li, L., Zhang, Q., Wang, Y., Terasaki, O., Yu, J., 2020. Subnanometer Bimetallic Platinum-Zinc Clusters in Zeolites for Propane Dehydrogenation. Angew. Chem. Int. Ed. 59, 19450–19459.

Sun, G., Zhao, Z.J., Mu, R., Zha, S., Li, L., Chen, S., Zang, K., Luo, J., Li, Z., Purdy, S.C., Kropf, A.J., Miller, J.T., Zeng, L., Gong, J., 2018. Breaking the scaling relationship via thermally stable Pt/Cu single atom alloys for catalytic dehydrogenation. Nat. Commun. 9, 4454.

Wang, Y., Hu, Z.-P., Lv, X., Chen, L., Yuan, Z.-Y., 2020. Ultrasmall PtZn bimetallic nanoclusters encapsulated in silicalite-1 zeolite with superior performance for propane dehydrogenation. J. Catal. 385, 61–69.

Wang, P., Yao, J., Jiang, Q., Gao, X., Lin, D., Yang, H., Wu, L., Tang, Y., Tan, L., 2022b. Stabilizing the isolated Pt sites on $PtGa/Al_2O_3$ catalyst via silica coating layers for propane dehydrogenation at low temperature. Appl. Catal. B-Environ. 300, 120731.

Wang, P., Liao, H., Yang, H., Lv, Q., Li, Y., Wu, L., Tang, Y., Xie, Z., Tan, L., 2023. Constructing PtCe cluster catalysts by regulating metal-support interaction via Al in zeolite for propane dehydrogenation. Chem. Eng. Sci. 269, 118450.

Wang, J., Liu, M., Li, J., Wang, C., Zhang, X., Zheng, Y., Li, X., Xu, L., Guo, X., Song, C., Zhu, X., 2022a. Elucidating the Active-Phase Evolution of Fe-Based Catalysts during Isobutane Dehydrogenation with and without CO_2 in Feed Gas. ACS Catal. 12, 5930–5938.

Wang, L.-C., Zhang, Y., Xu, J., Diao, W., Karakalos, S., Liu, B., Song, X., Wu, W., He, T., Ding, D., 2019. Non-oxidative dehydrogenation of ethane to ethylene over ZSM-5 zeolite supported iron catalysts. Appl. Catal. B-Environ. 256, 117816.

Wegener, E.C., Bukowski, B.C., Yang, D., Wu, Z., Kropf, A.J., Delgass, W.N., Greeley, J., Zhang, G., Miller, J.T., 2020. Intermetallic Compounds as an Alternative to Single-atom Alloy Catalysts: Geometric and Electronic Structures from Advanced X-ray Spectroscopies and Computational Studies. ChemCatChem 12, 1325–1333.

Wu, Z., Bukowski, B.C., Li, Z., Milligan, C., Zhou, L., Ma, T., Wu, Y., Ren, Y., Ribeiro, F. H., Delgass, W.N., Greeley, J., Zhang, G., Miller, J.T., 2018. Changes in Catalytic and Adsorptive Properties of 2 nm Pt_3Mn Nanoparticles by Subsurface Atoms. J. Am. Chem. Soc. 140, 14870–14877.

Xiong, H., Lin, S., Goetze, J., Pletcher, P., Guo, H., Kovarik, L., Artyushkova, K., Weckhuysen, B.M., Datye, A.K., 2017. Thermally Stable and Regenerable Platinum-Tin Clusters for Propane Dehydrogenation Prepared by Atom Trapping on Ceria. Angew. Chem. Int. Ed. 56, 8986–8991.

Yang, Z., Li, H., Zhou, H., Wang, L., Wang, L., Zhu, Q., Xiao, J., Meng, X., Chen, J., Xiao, F.S., 2020. Coking-Resistant Iron Catalyst in Ethane Dehydrogenation Achieved through Siliceous Zeolite Modulation. J. Am. Chem. Soc. 142, 16429–16436.

Yang, X., Liu, G., Li, Y., Zhang, L., Wang, X., Liu, Y., 2018. Novel Pt–Ni Bimetallic Catalysts $Pt(Ni)–LaFeO_3/SiO_2$ via Lattice Atomic-Confined Reduction for Highly Efficient Isobutane Dehydrogenation. Trans. Tianjin Univ. 25, 245–257.

Yang, W., Wang, Y., Zhou, J., Zhou, J., Wang, Z., Cen, K., 2017. Catalytic self-sustaining combustion of the alkanes with Pt/ZSM-5 packed bed in a microscale tube. Chem. Eng. Sci. 158, 30–36.

Yang, C., Wu, Z., Zhang, G., Sheng, H., Tian, J., Duan, Z., Sohn, H., Kropf, A.J., Wu, T., Krause, T.R., Miller, J.T., 2019. Promotion of Pd nanoparticles by Fe and formation of a Pd_3Fe intermetallic alloy for propane dehydrogenation. Catal. Today 323, 123–128.

Yang, M.-L., Zhu, Y.-A., Zhou, X.-G., Sui, Z.-J., Chen, D., 2012. First-Principles Calculations of Propane Dehydrogenation over PtSn Catalysts. ACS Catal. 2, 1247–1258.

Ye, C., Wu, Z., Liu, W., Ren, Y., Zhang, G., Miller, J.T., 2018. Structure Determination of a Surface Tetragonal Pt_1Sb_1 Phase on Pt Nanoparticles. Chem. Mater. 30, 4503–4507.

Yuan, F., Zhang, G., Zhu, J., Ding, F., Zhang, A., Song, C., Guo, X., 2021. Boosting light olefin selectivity in CO_2 hydrogenation by adding Co to Fe catalysts within close proximity. Catal. Today 371, 142–149.

Zhang, J., Deng, Y., Cai, X., Chen, Y., Peng, M., Jia, Z., Jiang, Z., Ren, P., Yao, S., Xie, J., Xiao, D., Wen, X., Wang, N., Liu, H., Ma, D., 2019. Tin-Assisted Fully Exposed Platinum Clusters Stabilized on Defect-Rich Graphene for Dehydrogenation Reaction. ACS Catal. 9, 5998–6005.

Zhang, X., Dong, J., Hao, Z., Cai, W., Wang, F., 2018b. Fe–Mn/MCM-41: Preparation, Characterization, and Catalytic Activity for Methyl Orange in the Process of Heterogeneous Fenton Reaction. Trans. Tianjin Univ. 24, 361–369.

Zhang, H., Liu, X., Zhang, N., Zheng, J., Zheng, Y., Li, Y., Zhong, C.-J., Chen, B.H., 2016. Construction of ultrafine and stable PtFe nano-alloy with ultra-low Pt loading for complete removal of CO in PROX at room temperature. Appl. Catal. B-Environ. 180, 237–245.

Zhang, G., Yang, C., Miller, J.T., 2018a. Tetrahedral Nickel(II) Phosphosilicate Single-Site Selective Propane Dehydrogenation Catalyst. ChemCatChem 10, 961–964.

Zhang, B., Zheng, L., Zhai, Z., Li, G., Liu, G., 2021. Subsurface-Regulated PtGa Nanoparticles Confined in Silicalite-1 for Propane Dehydrogenation. ACS Appl. Mater. Inter. 13, 16259–16266.

Zhu Chen, J., Wu, Z., Zhang, X., Choi, S., Xiao, Y., Varma, A., Liu, W., Zhang, G., Miller, J.T., 2019. Identification of the structure of the Bi promoted Pt non-oxidative coupling of methane catalyst: a nanoscale Pt_3Bi intermetallic alloy. Catal. Sci. Technol. 9, 1349–1356.

Zhu, J., Zhang, G., Li, W., Zhang, X., Ding, F., Song, C., Guo, X., 2020. Deconvolution of the Particle Size Effect on CO_2 Hydrogenation over Iron-Based Catalysts. ACS Catal. 10, 7424–7433.

Zhu, J., Wang, P., Zhang, X., Zhang, G., Li, R., Li, W., Senftle, T.P., Liu, W., Wang, J., Wang, Y., Zhang, A., Fu, Q., Song, C., Guo, X., 2022. Dynamic structural evolution of iron catalysts involving competitive oxidation and carburization during CO_2 hydrogenation. Sci. Adv. 8, eabm3629.